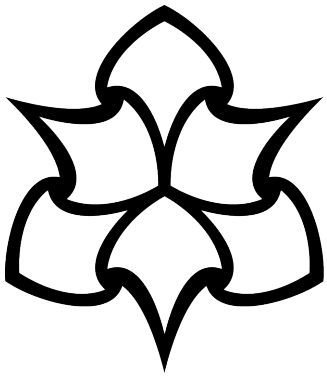

Received July 23, 2020, accepted July 26, 2020. Date of publication August 03, 2020, date of current version July 31, 2020.

Digital Object Identifier 10.1109/ACCESS.2020.3013967

Indoor Full-Body Security Screening: Radiometric Microwave Imaging Phenomenology and Polarimetric Scene Simulation

Neil A. Salmon[1], Senior Member, IEEE

[1]Department of Engineering, Manchester Metropolitan University, All Saints, Oxford Road, Manchester, M15 6BH, UK

e-mail: n.salmon@ mmu.ac.uk

This work was supported in part by the UK Department for Transport, Future Aviation Security Solutions (FASS) initiative.

ABSTRACT The paper discusses the scene simulation of radiometric imagers and its use to illustrate the phenomenology of full-body screening of people for weapons and threats concealed under clothing. The aperture synthesis technique is introduced as this offers benefits of wide field-of-views and large depths-of-fields in a system that is potentially conformally deployable in the confined spaces of building entrances and at airport departure lounges. The technique offers a non-invasive, non-cooperative screening capability to scrutinize all human body surfaces for illegal items. However, for indoor operation, the realization of this capability is challenging due to the low radiation temperature contrasts in imagery. The contrast is quantified using a polarimetric radiometric layer model of the clothed human subject concealing threats. A radiation frequency of 20 GHz was chosen for the simulation as system component costs here are relatively low and the attainable half-wavelength spatial resolution of 7.5 mm is sufficient for screening. The contrasts against the human body of the threat materials of metal, zirconia ceramic, carbon fiber, nitrogen-based energetic materials, yellow beeswax, and water were calculated to be ≤7 K. Furthermore, the model indicates how some threats frequency modulate the radiation temperatures by ~ ±1 K. These results are confirmed by experiments using a radiometer measuring left-hand circularly polarized radiation. It is also shown using scene simulation how circularly polarized radiation has benefits for reducing false alarms and how threat objects appear in canyon regions of the body, such as between the legs and in the armpits.

INDEX TERMS Airport, carbon fiber, ceramic, concealed weapons, contraband, knives, microwave, portal, radiometric.

I. INTRODUCTION

Microwave technology is gradually emerging and being acknowledged for its use in non-invasive screening for a wide range of metallic and non-metallic threats and illegal items concealed on persons under their clothing [1], [2]. At a time when the associated hardware and firmware costs are falling and digital signal processing algorithms are becoming ever more sophisticated, the system performance to cost ratio of portal systems gets closer to satisfying market expectations.

Exploitation of the near transparency of clothing to microwave and millimeter-wave radiation was first investigated for security screening in the late 1970s for the nuclear industry and law enforcement by the Sandia National Laboratories [3], [4]. Following this, a diversity of systems evolved, building on GaAs mixers and broadband amplifiers available in the 1980s. By exploiting receivers at and around 35 GHz and 94 GHz several impressive systems emerged for portal [5], [6], [7], [8], and stand-off [9] security screening of people.

Market expectations for microwave and millimeter-wave portals are that the whole body should be screened unobtrusively for all threats greater than about 1 cm in size in a matter of seconds. Ideally, this should be non-cooperatively in a volume of several cubic meters through which a subject would walk, without the requirement to remain motionless. Specific requirements on these systems set by governments, like probability of detection and false

This work was supported in part by the UK Department for Transport, Future Aviation Security Solutions (FASS) initiative.

alarm rate, will vary for the different screening scenarios such as entrances to airport departure lounges, transport networks, government buildings, schools, shopping malls, and arenas.

Microwave screening technologies fall into two basic categories, these being radars and radiometers. Radars illuminate a subject using one or more man-made point sources of coherent radiation and process the measured reflections into an image. Radiometers require no man-made sources as they image by focusing the natural thermal (or Planck) radiation from a subject on to a focal plane array. Alternatively, radiometers may use an array of antennas and receivers and create the image electronically using the aperture synthesis technique [10], as advocated in this paper. This technique is not limited by aberrations caused by focusing optics. As such this technique is more suited to the short ranges (10 cm to 2 m) of security screening portals.

Radar is the more mature technology with a range of high-quality products on the market operating at frequencies from a few GHz, right up to 80 GHz in the millimeter-wave band. Radar images are characterized by speckle (which is a graininess in the image) and dark regions that are not receiving sufficient illumination. Radiometry on the other hand offers the potential benefit of clarity in images but suffers in the indoor screening environment from low image contrast.

The problem of low contrast for indoor radiometric imaging is due to the low level of illumination, this effectively being the difference between the ambient temperature of the environment and the temperature of human skin. This temperature difference is of the order of 14 K and represents the maximum radiation temperature contrast that would be measured between a surface having a reflectance of unity and another having a reflectance of zero. However, for many threat materials and the human body, the reflectances have intermediate values and the contrasts in the imagery will be correspondingly smaller than 14 K. The severity of this contrast can be appreciated when it is realized that the noise in current imaging systems is somewhere in the region of 0.5 K to 2 K.

This paper presents a model of the clothed human in the indoor environment. This is used to determine the radiometric temperature contrasts between concealed threats under clothing and the adjacent clothed areas of the human body. Electromagnetic properties of materials are taken from referenced publications. Experimental measurements confirm the predicted radiation temperature contrasts. The results of the modeling and experiments are presented as tabulated numerical values and illustrated by scene simulation to show the phenomenology. This knowledge is important for the design of the next generation of aperture synthesis portal screening systems [11] which will use emerging powerful digital cross-correlators [12], [13], [14].

The following parts of the introduction explain more about the limitations of focal plane imaging radiometers for screening portals, why radar systems have dominated the market and the opportunities, and progress in the aperture synthesis systems for security screening. Section II of the paper describes the model used to predict the radiometric temperatures and the scene simulation technique. Section III presents the results of the model for various threats. Section IV describes experimental measurements of the radiometric temperatures of a selection of threat materials and the human body. Section V provides further details on how an aperture synthesis security screening portal may operate. Conclusions of the paper are provided in Section VI.

A. *FOCAL PLANE ARRAY RADIOMETRIC IMAGERS*

Using focal plane array (FPA) imagers is challenging for portal security screening in the microwave band, as the depth-of-field (DoF) is small. The DoF for an imager aperture size D at a subject range R in the near field ($R \sim D$) is limited [15] by the aberrations in the focusing lenses and mirrors to

$$\mathrm{DoF} = 4\lambda\left(\frac{R}{D}\right)^2, \qquad (1)$$

where λ is the radiation wavelength. Typically, this is 10 cm to 20 cm for FPA imagers, meaning a subject has to remain in a specific region whilst being screened. This is incompatible with walk-through portals and non-cooperative screening.

Two images taken with a well-designed system that optimizes the DoF are shown in Figure 1. It images circularly polarized radiation over the 28 GHz to 33 GHz band using a 58-channel FPA of radiometers [16], [17]. In the center of the field-of-view the spatial resolution is ~3 cm. However, in moving radially a distance of 10(20) cm from this point, the spatial resolution falls to 9(15) cm [18]. This is an example of how the DoF is limited in near-field imaging.

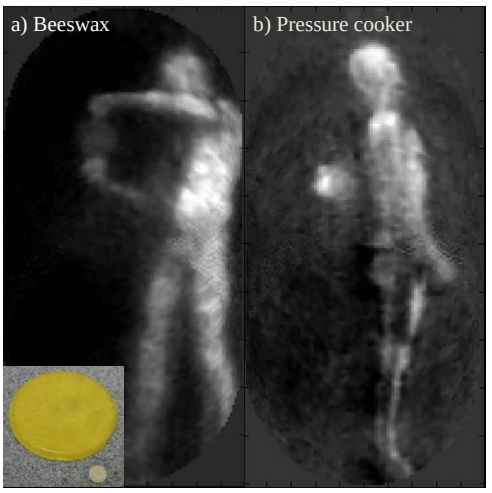

FIGURE 1. Experimentally measured images against an anechoic background of: a) an 17.5 cm diameter, 1 cm thick sheet of beeswax [16] (inset) and b) a metal pressure cooker inside a rucksack [17], generated by a 58-channel 31 GHz millimeter-wave imaging portal. White represents higher intensities of reflected illumination radiation.

Due to the small indoor radiometric temperature contrast, the level of illumination was enhanced by over one thousand man-made point source radiators distributed over a large area (~10 m^2). The system is something of a hybrid, as it combines the use of point source radiators (like a radar) with an imaging radiometer. The system demonstrated the detection of metal and non-metallic items concealed under clothing in an airport simulated environment. As such it reached level five on the Technology Readiness Level (TRL) scale. The first image from this system in Figure 1 shows a person holding a 1 cm thick circular disk of yellow beeswax, a surrogate material for a category of threats in the aircraft industry. It can be noted in the image that this object is only just detectable against the darker background.

The second image in Figure 1 illustrates that the transparency of a rucksack reveals the presence of the metal pressure cooker contained within. Although the system generates good imagery, the limited DoF means it can only image subjects in a relatively small volume.

The graininess in these images is a speckle pattern arising from the use of point sources of illumination. The pattern changes rapidly as the subject moves and as such is very difficult to remove. The level of speckle is close to that of the contrast of the beeswax when it is against the human body. As there appeared to be no clear way to reduce the level of the speckle, the system was deemed unsuitable for airport security screening, so its development was discontinued.

B. *IMAGING RADAR SYSTEMS*

Imaging radars, designed specifically to measure in the near-field, do not suffer the limited DoF of FPA imagers, as they focus the beams electronically. Consequently, several high-performance commercial systems are now available on the market [1], [2], [19]. The systems generate spectacular imagery by illuminating the subject with a coherent beam of radiation at a level much higher than the radiometric emission. Since systems only measure reflectivity, they have no sensitivity to the thermodynamic temperatures of objects in the scene, in contrast to that of radiometric imaging systems.

C. *APERTURE SYNTHESIS RADIOMETRIC IMAGERS*

Aperture synthesis imaging provides a solution to radiometric imaging in the near field, as it focuses the beam electronically; this gives the system an infinite DoF. The system uses an antenna-receiver array coupled to a cross-correlator, the output of which creates the images using beam-forming algorithms [10]. The principle is simple and it requires no man-made illumination. As the radiometric emission from the subject is incoherent, images are free from speckle effects that may otherwise generate false alarms. Potentially the technology could be used to image a walking subject, as images are generated at sub-millisecond timescales; no mechanical scanning is involved. Aperture synthesis for passive imaging in security screening has only been demonstrated in real-time in an indoor laboratory environment [20], [21], and has therefore only achieved level four on the TRL scale.

Two images from a proof-of-concept aperture synthesis imaging system [20] having 32-receiver channels, measuring horizontal linear polarization at 22 GHz, are shown in Figure 2. The first image (Figure 2a), in the near-field [22], is of a domestic iron covered with absorber at a temperature of 57°C at a range of 40 cm from the receiver antenna array against a 23°C ambient temperature background. Although the absorber has almost zero reflectance its presence is observed as its radiation temperature is higher than that of the background. The second image (Figure 2b), illustrates how the same system can image in the far-field with no changes to the hardware [20]; buildings have higher radiation temperatures, typically ~280 K, whilst the sky is radiometrically colder, typically in the region of 70 K at these elevation angles, with moderate cloud cover [23]. The 'noise' in the images arises mainly from the Fast Fourier Transform gridding and interpolation [22].

a) Domestic iron b) Public walkway

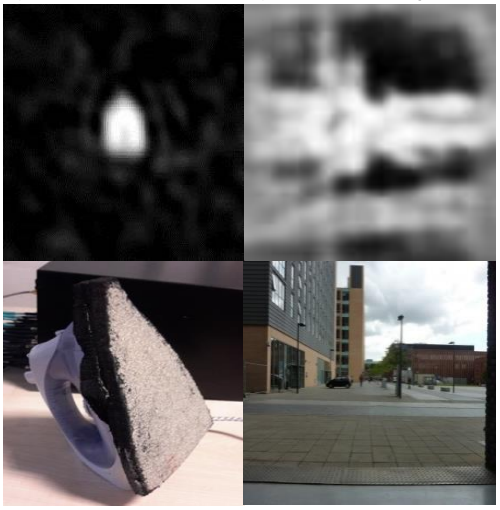

FIGURE 2. Images measured using a 32-channel 22 GHz aperture synthesis imager of: a) an absorber covered domestic iron at 57ºC against an ambient temperature (23ºC) background [22] b) an outdoor public walkway [20], white being radiometrically 'hot'.

D. *ENVISAGED SECURITY SCREENING PORTAL*

Dialogue with security screening operators indicates that threats or illegal items (such as contraband) are often concealed in bodily canyon regions such as in the armpits, between the legs, in the intergluteal cleft, and in other areas. For this reason, all regions of the body need to be exposed to the sensors of a screening system. The envisaged system of Figure 3 from [24] illustrates that by surrounding the subject with receivers all skin areas of a walking person can be measured, leaving no area without analysis and interpretation.

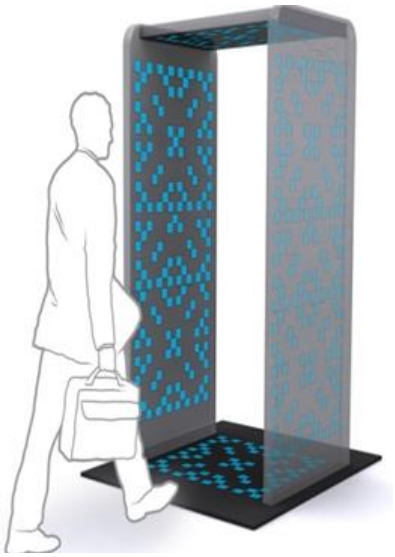

FIGURE 3. The envisaged walk-through aperture synthesis 3-D imaging radiometric aperture synthesis security screening portal [24]. The portal may contain hundreds of antennas and receivers distributed randomly over the inside surfaces.

A variation on that in Figure 3 might require a wider walkway, enabling subjects to transit the portal with arms held out to the side, so under-arm areas can be screened. Baggage carried by subjects would need to be screened separately. The hardware challenge, in realizing this capability, is the development of cost-effective antenna arrays with hundreds of multi-GHz bandwidth receivers linked to digital cross-correlators. Software challenges are to find efficient near-field image creation algorithms to process the cross-correlations and to use machine learning to recognize potential threat items in a matter of seconds. This technology would complement other emerging technology to combat the proliferation of terrorism [25].

II. RADIOMETRIC PORTAL MODELING THEORY

A. *THE RAY-TRACING MODEL*

A radiometric ray-tracing model, initially described in [23], is extended here to simulate indoor security screening of people concealing threat items under their clothing. The subjects and the threat items used in the simulations come from three-dimensional computer graphics models, these contain thousands of facets having sizes down to millimeter scales.

Pencil beam rays emanating from a hypothetical imager adjacent to the subject make a 1.0 m by 2.0 m raster scan of the portal containing the 1.8 m tall subject and their background. As each ray travels through space, both the emission and the absorption along the line of sight are calculated. When a ray encounters a facet, the facet direction normal and the direction vector of the ray are used to calculate the polarimetric components of reflectivity. At each facet the ray splits into two, one reflected and one transmitted. At this point, the polarimetric intensities of the reflection, emission, and transmission are summed, as indicated by (2). A search algorithm is then used [26] to find the next facet that is intersected by the ray. The algorithm used to make these calculations is recursive, so any number of reflections along a single ray path can be handled. For practical purposes it was found that only two reflections from the human body are necessary to model radiation temperatures from the canyon regions [27], so the ray tracing finishes after two facet interactions. Following this, any residual emission from the ambient temperature background is added.

A radiation frequency of 20 GHz was chosen for the simulation. This is because it would provide good image spatial resolution (~7.5 mm) in a portal configuration, where the subject is viewed from all directions by antennas and the spatial resolution becomes half the wavelength [11]. The radiation bandwidth of the receivers is assumed to be 2 GHz, to give good radiometric sensitivity.

Rays are raster-scanned over the subject with a 3 mm step size to create a rendered image. This image is then convolved with a point spread function that has a full width at half maximum of 7.5 mm, this simulating the resolution that would be achieved in the portal.

Reasonable assumptions used in the model are based on experimental knowledge and are the following. There is no emission or absorption in the air surrounding the subject, this means the range step size in the ray-tracing can be just the imager to subject distance. Reflections from threats and the human body are purely specular and there is no polarization scrambling as indicated in [28]. Clothing, threat items, and the human body can be treated radiometrically as three parallel layers.

The model has been developed in the Interactive Data Language (IDL), a compiler-based interpreter language. Finer details of the simulation model are included in the following sections of the paper.

B. *RADIOMETRIC TEMPERATURES*

In the microwave band where $hf < kT_S$ (h being Planck's constant and k being Boltzmann's constant), the intensity of thermal emission is proportional to $T_S E_S$, the product of the thermodynamic temperature, T_S and emissivity, E_S of the object. For all objects the emissivity ranges from zero to unity; zero for an object which is 100% reflective and unity for one which reflects nothing (and is completely absorbing). For an object which is non-transmissive, the emissivity is given by $E_S = 1\text{-}\Gamma_S$, where Γ_S is the object reflectance.

A radiometric sensor measures the radiometric temperature of objects T_{RAD} in Kelvin. Generally, this comprises three contributions: 1) environmental radiation reflected from the object; 2) direct emission from the object and 3) any transmission through the object. Mathematically, the radiometric temperature of the object is

$$T_{RAD} = T_I \Gamma_S + T_S E_S + T_B \Upsilon_S \,, \tag{2}$$

where T_I is the illuminating radiation temperature on the front of the object, Υ_S is the transmittance of the object and

T_B is the background illuminating radiation temperature on the reverse side of the object. In many cases the transmittance of an object is zero, leaving only the first two terms in this equation.

C. *RADIOMETRIC SENSITIVITY*

To appreciate the difficulty associated with the small indoor radiation temperature contrast, the noise in these systems needs to be quantified. Together these constitute the signal to noise ratio. The minimum detectable radiation temperature is given by the radiometer equation

$$\Delta T = \frac{T_A + T_R}{\sqrt{B_{RF} t_{INT}}} \left(\frac{1}{F \eta_Q \eta_M} \right), \quad (3)$$

where T_A is the average radiation temperature in the scene (referred to as the antenna temperature) and T_R is the receiver noise temperature. The radiation bandwidth is given by B_{RF}, t_{INT} is the integration time, F is the fractional filling factor of the receiver antenna array, η_Q is the digitization quantization efficiency and η_M is the antenna main beam efficiency. For focal plane array systems, the fractional filling factor is unity, as is η_Q.

For aperture synthesis systems the filling factor maybe a few percent to tens of percent, dependent on other factors such as the antenna array configuration and the radiation bandwidth, as described below. In the proof-of-concept aperture synthesis system [20] used to generate images in Figure 2 the radiation bandwidth is 300 MHz, the antenna temperature is 290 K and the receiver noise temperature is 463 K. The fractional filling factor is 23%, the quantization efficiency is 0.64 and the main beam efficiency is 0.7, giving a minimum detectable radiation temperature of 0.5 K for a one second integration time and 2 K for a 25 ms integration time. If the radiation bandwidth in this system were increased to 10 GHz, the same radiometric sensitivity could be achieved with a 4.0% antenna filling factor. Future systems are likely to require radiometric sensitivities in the region of 100 mK, if non-metallic threats are to be reliably recognized in future security screening portals.

D. *ANTENNA ARRAY TOPOLOGY*

The requirements of the antenna array are two-fold, firstly to collect sufficient radiation to obtain the desired radiometric sensitivity as dictated by (3) and secondly to collect sufficient information to create an alias-free diffraction-limited image. In the aperture synthesis technique, spatial frequencies of the scene are sampled by cross-correlating radiometric electric fields at the locations of pairs of antennas. To avoid aliasing, all spatial frequencies must be sampled [11] by using antenna separations (baselines) from a minimum half-wavelength spacing (equivalent to Nyquist spatial sampling of the radiation field), right up to the maximum separation allowed by the full aperture [29].

A category of antenna arrays that sample all spatial frequencies with the minimum number of antennas is referred to as a minimally redundant array. The cost implications of selecting such arrays should now be apparent. Research has indicated that antennas on hexagonal grids are superior to those on square grids, as they have a more symmetric beam pattern, with lower sidelobes and require fewer antennas [30]. Simulation also shows that a small amount of randomization in the positions of antennas on a less than redundant hexagonal grid array disperses the effects of aliasing in the image [31]. Techniques developed to minimize the redundancy of linear arrays, whilst maximizing the radiometric sensitivity and optimizing the angular resolution are presented in [32] [33] [34]. It is intended that this technique would be extended to two-dimensional arrays.

Tiles of minimally redundant arrays might be used in a modular form in a future aperture synthesis security screening portal to build up the complete array. This is somewhat similar to the transmit-receiver tiles used in the active (radar) security screening portals [2], [19].

E. *APERTURE SYNTHESIS IMAGING ALGORITHMS*

The aperture synthesis imaging technique of radio astronomy has been adapted to generate three-dimensional (3-D) images in the near-field, where the spatial resolution of this technique has been demonstrated to be that of the Abbe microscope [11]. This resolution is ~ λ/2 for a portal configuration, where the subject is surrounded by receiving antennas. There is potential to enhance this resolution by using the Gerchberg technique [22], where positional information about a subject is provided to the image creation algorithm.

F. *OPTIMUM OPERATIONAL RADIATION FREQUENCY*

Since an aperture synthesis system in a portal configuration has the ~ λ/2 Abbe microscope resolution, operation at 20 GHz gives a spatial resolution of ~ 7.5 mm which is considered sufficient to resolve many threats.

In comparison to the higher frequencies in the millimeter-wave band, the cost of technology at 20 GHz is relatively low and has higher performance. Furthermore, higher frequency systems are required to have larger numbers of channels, to satisfy Nyquist spatial sampling of the radiometric electric fields; the number of channels rises with the square of the frequency. Furthermore, the complexity of the correlator of an aperture synthesis imager rises as the square of the number of receiver channels, so there are severe cost penalties in moving to higher radiation frequencies.

Moving to frequencies below 20 GHz might offer an attractive cost saving due to the smaller number of receivers and the less powerful correlator that would be required. However, the spatial resolution at half a wavelength would mean only larger threat items could be recognized. For example, at 3 GHz the spatial resolution would only be 5 cm.

It may be advisable when selecting an operational frequency band to consider the users of the radio spectrum

which may be transmitting in these bands, as this may lead to interference in the operation of a passive imager. Permitted usage in the bands is indicated in the respective national frequency allocation tables. However, the use of microwave absorber in systems can in many cases attenuate interfering emissions to levels well below that of the radiometric emission.

G. *SUBJECT ILLUMINATION*

In the simulations of this paper, it has been assumed that the thermodynamic temperature of the environment of the portal is 295.15 K, which is the case if the building heating thermostat is set to 22°C and the portal is isolated from 'cold' outdoor environmental microwave emission entering through windows and open doors. This isolation can be arranged by suitable geometry of absorbing surfaces around the portal, preventing the likelihood of spurious reflections, which may otherwise generate false alarms. Under these conditions, the illuminating radiation temperature from all directions in the portal can be guaranteed to be at 295.15 K. These simulation conditions have also been selected as they are those conditions under which the experimental measurements were made.

H. *POLARIZATION SIGNATURES*

Since there is little or no chirality in materials of interest for security screening, there are no great differences between radiometric emissions in the right- or left-hand circular polarizations. Although a predominance of right over left-hand circular polarimetric emission (or vice versa) can be generated by two consecutive reflections from non-chiral materials, measurements of the Stokes' Parameters (S_0, S_1, S_2, S_3) in radiometric microwave imaging indicates [28], [35], [36] that the last Stokes' Parameter is smaller than a few percent of the first. This does not mean that there is no emission into the right or left-hand circular polarizations, only that their intensities are approximately equal. Assuming they are equal, conservation of energy dictates the intensity of the circular polarizations will be the average of the orthogonal linear polarizations (these being the normal (N) and parallel (P) linear polarizations) and this has been used in the model to calculate the intensity of the circular polarization.

Since references [28], [35], [36] indicate the degree of linear polarization (the predominance of N over P) may be up to ~17%, linear polarization effects need to be included in the model. This has been done by using the Fresnel Equations as discussed in the next section.

I. *LAYERED STRUCTURES IN TARGETS*

In the region below about 25 GHz, most clothing becomes effectively transparent, whilst some threat items become semi-transparent and others remain opaque. This means the clothed human body together with that of concealed threat items can be modeled using layers of radiating and reflecting materials, first developed to model the signatures of the surface of the earth in the microwave band for remote sensing [37].

The earth layer models were adapted to model the layers of clothing and threat items concealed under the clothing against the body [38]. The models take into consideration the multiple reflections between the layers. Experimental evidence indicates that below ~100 GHz human skin behaves as a specular reflector, which simplifies the modeling [28]. Since the majority of objects are larger than the radiation wavelength, to first order, scattering can be neglected. For objects with dimensions on the order of the wavelength, or smaller, scattering can be included by increasing the solid angle into which illumination is reflected from objects, as described in [39].

At a flat interface of two media the specular amplitude reflection coefficients of the N and P linear polarizations are given by the Fresnel equations:

$$\rho_N = \frac{\eta_2 cos\theta_1 - \eta_1 cos\theta_2}{\eta_2 cos\theta_1 + \eta_1 cos\theta_2} \tag{4}$$

$$\rho_P = \frac{\eta_2 cos\theta_2 - \eta_1 cos\theta_1}{\eta_1 cos\theta_1 + \eta_2 cos\theta_2} \tag{5}$$

where $\eta = \sqrt{\mu_r/\epsilon_r}$ is the intrinsic impedance of the medium, μ_r and ϵ_r are the respective complex relative permeability and permittivity, and θ_1 and θ_2 are the incidence and refraction angles given by Snell's law $sin\theta_2/sin\theta_1 = n_1/n_2$ where $n = \sqrt{\mu_r \epsilon_r}$. From these the intensity (or power) reflectance coefficient is just given by the complex square $\Gamma = \rho\rho^*$.

In propagating through a medium the electric field of the wave is described by $e^{j(\omega t - \beta z)} e^{-\alpha z}$ where $\alpha = \omega n''/c$ describes the field attenuation and $\beta = \omega n'/c$ describes the phase effects, $n = n' - jn''$ being the complex refractive index of the medium. When propagating at an angle θ_L through a medium of thickness d, the power loss becomes $L = \exp(2d\alpha/cos\theta_L)$.

For a layer of material bound by two interfaces the composite field (or amplitude) reflectivity is given [37] by

$$\rho_L = \frac{\rho_1 + \frac{\rho_2}{L} e^{-j\beta d/cos(\theta_L)}}{1 + \frac{\rho_1 \rho_2}{L} e^{-j\beta d/cos(\theta_L)}}, \tag{6}$$

which accounts for the combined reflection from both interfaces and the absorption from the material between. Similarly, the transmission τ_L of the layer can be obtained, as presented in [27].

For the power (intensity), the reflectance is $\Gamma = |\rho_L|^2$ and transmittance is $\Upsilon = |\tau_L|^2 \eta_T cos\theta_T/\eta_I cos\theta_I$, where τ_L is the layer transmission, and subscripts *I* and *T* refer respectively to the medium above and below the layer. The emissivity (or absorptance) E of the layer can then be found from the conservation of energy, which is

$$1 = \mathrm{E} + \Gamma + \Upsilon. \quad (7)$$

The response of materials to electromagnetic waves is described more simply by the complex refractive index. However, when measuring materials very often it is the relative permittivity that is measured and documented. For all the materials of interest here at these frequencies, it is sufficient to assume that the complex relative permeability μ_r is unity, with no imaginary component. Under these conditions, the relationship $n = \sqrt{\epsilon_r}$ relates the complex refractive index to the complex relative permittivity, this being given by $\epsilon_r = \epsilon_r' - \epsilon_r''$, where ϵ_r' and ϵ_r'' are the real and imaginary components respectively. By combining multiple layers in a fashion outlined in [37] it is possible to describe a composite amplitude reflectivity by a summation from the different layers, the squaring of which gives the coherent reflectance. Similarly, by summing the intensities from the multiple layers the incoherent reflectance can be determined. In the layer models, each layer is characterized by a thickness, a complex relative permittivity, and a temperature. The radiation temperatures of the background and concealed threats in this paper are calculated using (2), where the reflectance Γ is taken from the above model.

In the coherent model, there is variation in the intensity taking the form of interference fringes which can only be observed if the system radiation bandwidth is much narrower than the fringe spacing and the layers are perfectly parallel. In practice, neither of the conditions will be completely satisfied. On the other hand, the incoherent model assumes no wave coherence, which would only be true if the layers had very rough surfaces (in relation to the wavelength) and the radiation bandwidth was far greater than the fringe spacing. These facts are also unlikely to be true. In a measurement scenario, the reality will fall somewhere between the coherent and incoherent models, so in these simulations, both cases are shown.

III. RADIOMETRIC PORTAL MODELING RESULTS

A radiation transport model is presented here which analyses the performance of security screening portals. The results are presented in tabular form and as ray-tracing scene simulations. Together these enable the performance capability of the security screening portal to be assessed.

Scene simulations offer an assessment and evaluation tool for new security screening deployment scenarios, like crowd surveillance and walk-through portals. The scene simulation model presented in [23] was therefore extended to include multiple bounce modeling of reflections [27], so that canyon regions (underarms and between legs) could be described, where higher radiation temperatures have been measured than could be accounted for using a single bounce model. These regions are of particular interest in security screening, as it is exactly in these places where criminals conceal threats and illegal items. Rendered images are convolved with the point spread function of the sparse antenna array. In the near field, this results in a spatial resolution of around half the wavelength (~ 7.5 mm) [11]. Gaussian noise equivalent to a radiation temperature of 100 mK can then be added to each pixel to represent realistic system parameters for security screening. However, the scene simulations, this was reduced to a few mK to show better the results.

A. *THE CLOTHED HUMAN BODY – THE BACKGROUND*

As the clothed human body represents the background to the target, it is important to have a good understanding of the signature of the body alone. In the following simulations, the background human body has an assumed height of 1.8 m.

The relative permittivity of the human body has been measured and modeled over the microwave and millimeter-wave band [40], [41], [42], [43], so electrically its response is well understood. Furthermore, measurements have also shown that in the microwave band properties of reflectance and emissivity of human skin vary by up to ±15% [44]. These vary with age, gender, ethnicity, and the particular part of the body under consideration. For modeling human skin in this work, the real and imaginary parts of the relative permittivity (ϵ_r', ϵ_r'') have been taken to be (15.53, 15.94). This was taken from the data in [43] for a radiation frequency of 20 GHz, giving bare skin a reflectance of 46% at normal incidence, as indicated in Table I.

The properties of clothing have been measured by several researchers [45], [46], [47], [48], [49]. Although many of these measurements are just slightly above 20 GHz, the trend is higher transmission at lower frequencies. A figure for the relative permittivity of clothing that reproduces the results in the 20 GHz to 30 GHz band is (1.5, 0.05) [49]. This, therefore, is the value taken for the simulations presented in this paper. When a clothing thickness of 5 mm is taken, this gives a transmittance of 90%, and absorptance (or emissivity) of 1% and a reflectance of 9%, as illustrated in Table I. Leather having a thickness of ~1.3 mm was measured [49] to have a 90% transmittance at normal incidence in free space at 20 GHz. Thicker clothing and leather types are somewhat more absorbing and reflective, particularly when they are damp from perspiration or wet from precipitation.

The geometry of the layer model used in the simulation is illustrated in Figure 4. For the background (clothed human body) a 5 mm thick layer having a relative permittivity of (1.5, 0.05) covers the skin of the body which has an assumed relative permittivity of (15.53, 15.94) [43]. The clothing has been assumed to have a thermodynamic temperature of 295.15 K, the same as that of the environment. Although the body and the clothing have been assumed to be flat, the model gives [38] surprisingly good results, even though clothing is wrinkled and with air pockets.

The skin of the human body has been assumed to have a thermodynamic temperature of 308.85 K (35.7°C). This is

TABLE I

RELATIVE PERMITTIVITIES OF THE HUMAN BODY, CLOTHING, AND THREAT MATERIALS TOGETHER WITH THEIR MODELED RADIATION TEMPERATURES OF CIRCULAR POLARIZATION AT 20 GHz, ILLUSTRATING COHERENT (AND INCOHERENT) EFFECTS AT NORMAL INCIDENCE FOR AN ENVIRONMENTAL ILLUMINATION RADIATION TEMPERATURE OF 295.15 K (22°C) AND A HUMAN SKIN THERMODYNAMIC TEMPERATURE OF 308.85 K (35.7°C).

Material	Relative permittivity ε_r or reflectance Γ	Thickness	Transmittance, emissivity, reflectance in air at normal incidence	Reflectance (under clothing against the human body) at normal incidence	Radiation temperature at normal incidence	Radiation Temperature Difference (Target – Background)
Human Body (bare skin) [43]	ε_r ~ (15.53, 15.94)	>10 cm	0.000, 0.544 0.456 (0.000, 0.544 0.456)	No clothing No target	302.6055 K (302.6055 K)	N.A.
Clothing on human body [45], [49]	ε_r ~ (1.5, 0.05)	5 mm	0.9041, 0.0857, 0.0102 (0.9000, 0.0814 0.0186)	0.3575 (0.3233) No target	302.7606 K (302.9295 K) Background	0.0 K (0.0 K)
Metal (specular)	Γ =100 %	>1 μm	0.0, 0.0, 1.0 (0.0, 0.0, 1.0)	0.8771 (0.8396)	295.1704 K (293.1720 K)	-7.59 K (-7.59 K)
Carbon fiber knife blade [50]	ε_r ~ (6.0, 3.0)	1.1 mm	0.3308, 0.2637, 0.4055 (0.3656, 0.3809, 0.2535)	0.1100 (0.1444)	303.5290 K (303.1990 K)	+0.7684 K (+0.269 K)
Ceramic knife (Zirconia) [51]	ε_r ~ (30.0, 0.1)	1.6 mm	0.3520, 0.0081, 0.6399 (0.3467, 0.0114, 0.6419)	0.4871 (0.3571)	300.9014 K (302.3567 K)	-1.8592 K (-0.5728 K)
RDX [52]	ε_r ~ (3.0, 0.02)	5 mm	0.9076, 0.0247, 0.0677 (0.8452, 0.0238, 0.1310)	0.3724 (0.2248)	302.4225 K (304.2253 K)	-0.3381 K (+1.2958 K)
		10 mm	0.7794, 0.0430,0.1776 (0.8248, 0.0470, 0.1282)	0.2018 (0.2444)	303.3332 K (304.1971 K)	+0.5726 K (+1.2676 K)
Yellow beeswax [53] (simulant)	ε_r ~ (2.36, 0.015)	5 mm	0.9758, 0.0226 ,0.0016, (0.8959, 0.0200, 0.0841)	0.3581 (0.2495)	302.6196 K (303.8309 K)	-0.1410 K (+0.9014 K)
		10 mm	0.9524, 0.0429, 0.0052 (0.8776, 0.0400, 0.0824)	0.3591 (0.2419)	302.5070 K (303.8309 K)	-0.2536 K +0.9014 K
Water pack at 28.85°C [54]	ε_r ~ (48.7085 32.7862)	10 mm	0.00, 0.395 0.605 (0.00, 0.395 0.605)	0.4986 (0.4571)	297.9108 K (298.0328 K)	-4.8498 K (-4.8967 K)

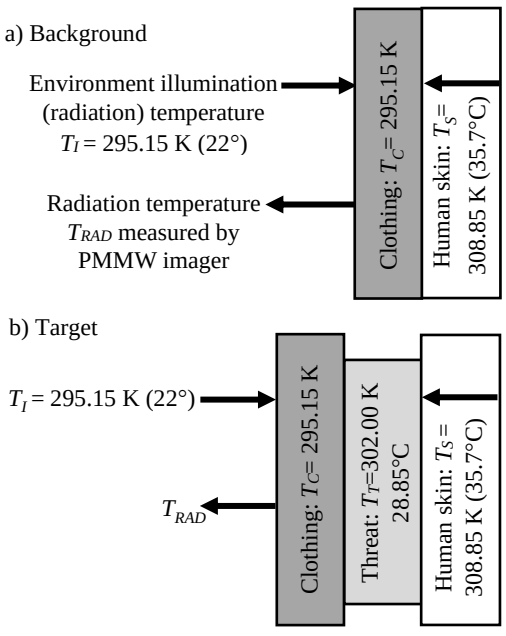

FIGURE 4. The layer model of a) the background (clothed human) and b) the target comprising the threat sandwiched between the clothing and the skin of the human body.

quite reasonable for a fully clothed person in an indoor environment, although it may well vary between much lower values in cold weather and up to 36°C when thicker clothing is worn. The thermodynamic temperature of the threat has been assumed to be the average of the skin and environment thermodynamic temperature, a value of 302.00 K (28.85°C).

Putting the clothing over the human body results in a composite response and this can be described by the layer model. The results of this for the coherent and incoherent models at 20 GHz are discussed in the next section and summarized in Table I.

1) RADIATION FREQUENCY VARIATION

The variation in the radiation temperature with frequency for the fully clothed human from 10 GHz to 80 GHz is shown in Figure 5, so comparisons can be made with real receivers operating over this band. The radiation temperature at 20 GHz is in the region of 302.8 K. The simulation also shows there are differences between the coherent and incoherent layer models.

The coherent model illustrates a sinusoidal modulation in the radiation temperature of ±1 K with frequency, which is caused by the constructive and destructive interference associated with the etalon effects in the clothing, referred to as radiometric fringes. The frequency spacing of the fringes

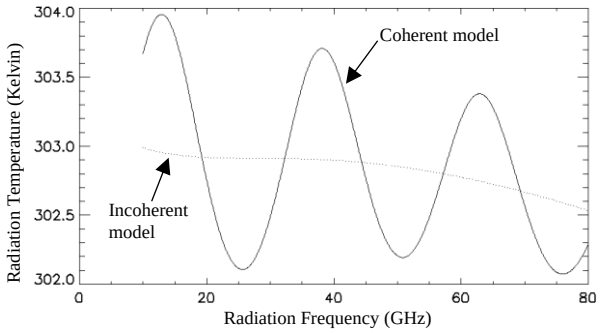

FIGURE 5. The radiation temperature of the clothed human subject as a function of frequency showing results for the coherent (solid line) and incoherent (dotted line) layer models at normal incidence.

is given by $\Delta f = c/(2n'dcos\theta)$, where n' is the real part of the refractive index, d is the clothing thickness and θ is the angle of incidence, taken to be 0° for normal incidence in the case of Figure 5. This gives a fringe spacing of ~25 GHz, for the refractive index n' of 1.225 and a thickness of 5 mm. With thinner clothing the fringe spacing increases. In practice, the fringes may become 'washed out', due to variations in the thickness of clothing and the angles of incidence or the use of very wide radiation bandwidth radiometers. In these cases, the radiation temperatures may look more like those of the incoherent model.

Both the coherent and incoherent models show a gradual fall in the radiation temperature by about 0.5 K in the region from 20 GHz to 80 GHz, this being a result of competing effects of the fall in the reflectivity of the human body (due to lower values of permittivity) and the rise in the emission from clothing (due to its greater absorption).

2) OBSERVATION ANGLE VARIATION

The variation in the radiation temperature with observation angle, ranging from normal to glancing incidence, for the clothed human body for the incoherent model is displayed in Figure 7.

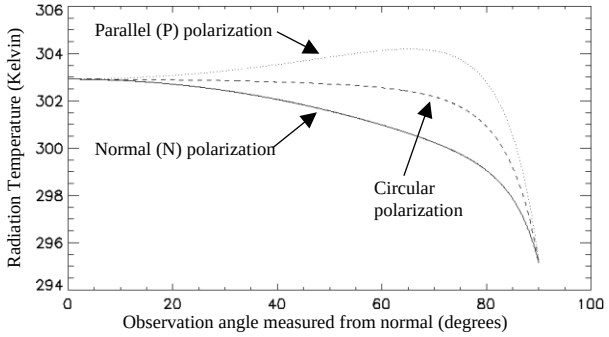

FIGURE 7. The radiation temperature in the normal (N or S) polarization (solid-line), parallel (P) polarization (dotted line), and circular polarization (dashed line) as a function of observation angle for the fully clothed human modeled with the incoherent layer model.

The main features of the response shown in Figure 7 are that as the observation angle is increased to around 70° the radiation temperature of the parallel (P) polarization rises from 302.9295 K to 304.1971 K, whilst that of the normal (N or S) polarization falls and that of the circular polarization remains relatively constant. This effect in the P-polarization is a manifestation of the Brewster angle effect, where the reflectance falls to a minimum at the Brewster angle and as a result, the radiation temperature reaches a maximum. As the observation angle increases toward 90°, the radiation temperatures in all polarizations fall to that of the illuminating background radiation temperature of 295.15 K. This is because the Fresnel reflectance approaches unity at glancing incidence. A similar variation is displayed for the coherent model, but for brevity is not shown.

The smaller variation in the radiation temperature in the circular polarization out to about 75° is a valuable attribute for security screening, as this means there will only be small variations in the radiation temperature of the background human form. This is an asset for machine interpretation, as it will lead to fewer anomalies that would otherwise generate false alarms; measuring the circular polarization effectively reduces the amount of clutter in the image. The effect can be demonstrated using the scene simulation model and this is displayed in Figure 6.

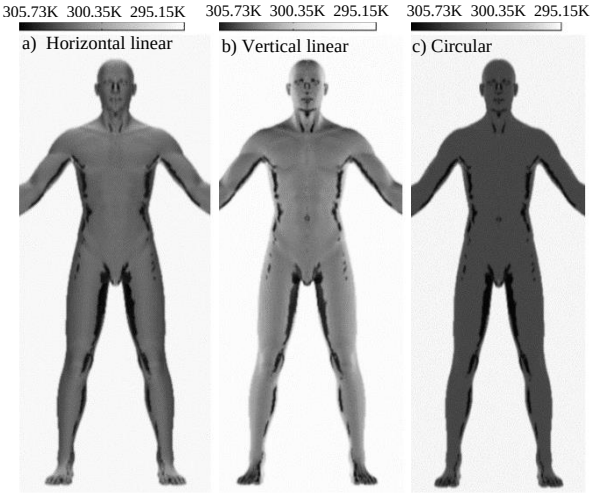

FIGURE 6. Scene simulation of an image of a person at 20 GHz illustrating the effects in a) horizontal linear, b) vertical linear and c) circular polarization. The Brewster angle reflection and body canyon illumination effects can be observed. The radiometric temperature is on the scale above the image; black represents radiometrically 'hot'.

The following scene simulations have been made using the coherent model. This was chosen, in preference to the incoherent model, as the fringe spacing, related to the clothing and threat thickness, is much greater than the assumed ~2 GHz radio frequency bandwidth of the radiometer. This is also the approximate bandwidth of the instrument used to make the measurements. For much larger bandwidths ~20 GHz, approaching the fringe spacing, the incoherent model would be more appropriate.

3) BACKGROUND SCENE SIMULATION

The scene simulation of a fully clothed person as background with no threats on the body is shown in Figure 6. From left to right the images represent the horizontal linear (HL), vertical (VL), and circular polarization. The main features in the image are the dark areas (307.0 K) in comparison to the remainder of the body which has a radiation temperature of 302 K. The dark areas are a result of the illuminating radiation already having been reflected from a region of the human body. Consequently, this radiation has a higher radiation temperature than it would have, if it were to have originated directly from the 'colder' surrounding environment. This effect can be seen on the sides of the torso, under the arms, between the legs and in the regions around the neck. This phenomenon has been observed in measured images of people [27] and is referred to as the canyon illumination effect.

Noticeable in areas away from the canyon regions are the Brewster angle effects. In the HL polarization, the vertical areas of skin at the sides of the body are seen with higher radiation temperatures than the horizontally forward sloping areas. The reverse is true in the VL polarization, with the horizontal forward sloping areas of skin having higher radiation temperatures than the vertical sides. The curvatures arising from body shape, muscle, and fat modulate the radiation temperatures by ±1 K, as can be seen in the images of Figure 6 and the plots Figure 7. These are not helpful when trying to identify potential threats.

The scene simulation image in circular polarization shows none of the above Brewster angle effects and as a result, the temperature across the body appears more or less uniform at around 302.8±0.1 K, a fact supported by the plot of Figure 7. This is ideal for security screening, as the absence of any such variation minimizes the chances of false alarms in machine analysis of imagery. Reception of circularly polarized radiation, in a system that would otherwise receive linearly polarized radiation, can be achieved by placing a quarter-wave plate in front of the receiver. Dependent on the orientation of the quarter-wave plate fast-axis, either left or right-hand circular polarization will be measured. Alternatively, circularly polarized radiation can be measured by using a stepped septum-type waveguide circular polarizer on the front-end of a radiometer sensitive to linear polarized radiation. The use of such a system is described in the supporting experimental measurements section of this paper.

B. *A SELECTION OF THREAT ITEMS*

Since microwave technology is capable of detecting both metal and non-metallic threats, several threat materials have been identified for simulation and their properties are presented in Table I. Since metallic threats by way of knives, guns and bombs constitute serious threats, their material properties are shown for comparison.

All threats appear with radiation temperatures between ~293 K and ~304 K, whilst that of the clothed human body appears at 302.8 K. The contrast in the images is just the modulus of the difference between these two levels, this being 9.8 K and 1.2 K. This is a small and challenging contrast for existing radiometric imagers to measure with any precision over the whole of the body in a matter of seconds. It is small because the temperature difference between human skin 308.85 K (35.7°C) and the indoor central heating temperature 295.15 K (22°C) is also small.

Scene simulations showing the physical appearance of the threats are shown in Figure 8. These simulations have been made using the incoherent layer model and for emission in the circular polarization. These simulations are the same as those shown in Figure 6 except that the arms of the person have been raised so canyon effects at the sides of the body are eliminated. The results of these simulations are now discussed in detail.

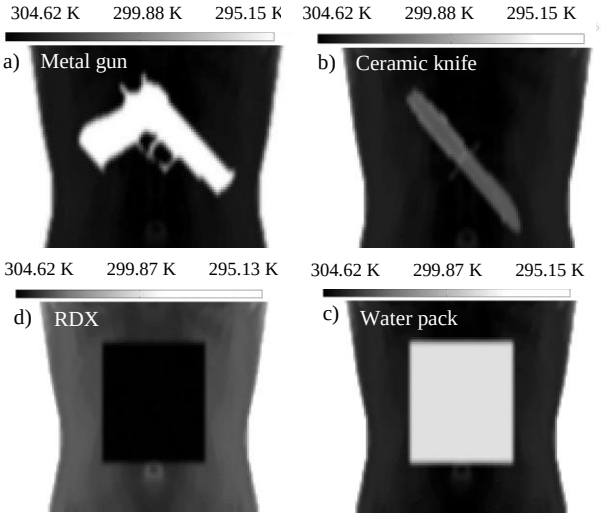

FIGURE 8. Simulated images in circular polarization using the incoherent layer model, clockwise from top left: a) metal gun, b) 1.6 mm thick ceramic knife, c) 5 mm water pack, d) 10 mm sheet RDX. Radiation temperatures in Kelvin for each image are illustrated in the scale at the top of each image.

1) METAL PISTOL

The simulation shows an image of a 20 cm long metal pistol. The estimated radiation temperature of this target is 295.17 K, just slightly above that of the environment illumination radiation temperature of 295.15 K, because of a small amount of emission from the layer of clothing. Metal presents the largest signature against the human body background body, due to its unity reflection coefficient.

2) CERAMIC AND CARBON FIBER KNIVES

Simulations are made for knives which are 20 cm long. The carbon fiber [50] knife has a thickness of 1.1 mm and appears with a radiation temperature of 303.52 K, as shown in Table I. The ceramic (ZrO_2 zirconium dioxide referred to as zirconia) [51] knife has a thickness of 1.6 mm and a radiation temperature of 300.90 K. The reflectivities of these materials are less than that of metal and the contrast between these threats and the human body is correspondingly smaller, as can be seen in Figure 8 for the ceramic knife. A plot of the

variation in the radiation temperature of the ceramic knife as a function of radiation frequency for the coherent and incoherent layer model is illustrated in Figure 10. The variation in the radiation temperature from the coherent layer model is ±2K. The fringes in this case, are composite, being partly due to the clothing and partly due to the knife blade thickness. The fringes, referred to as radiometric cavity fringes, might be used to identify anomalies on the human body for security screening.

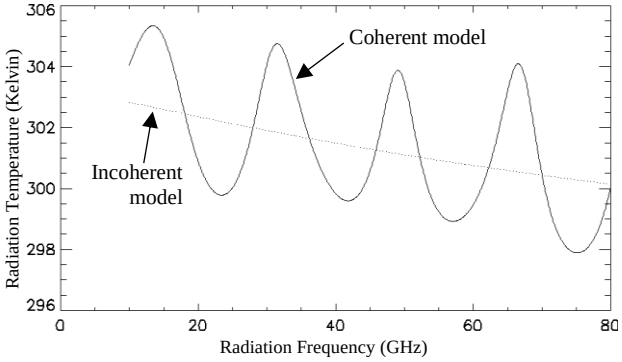

FIGURE 10. The radiation temperature as a function of radiation frequency for a 1.6 mm thick ceramic knife blade against the body and concealed by a 5 mm thick layer of clothing from the coherent (solid) and incoherent (dotted) layer models at normal incidence.

3) RDX

Typical of the nitrogen-based energetic materials is Royal Demolition Explosive (RDX), also referred to as cyclonite. This has [52] a relative permittivity of (3.0, 0.02), and the model predicts this to have a radiation temperature of 303.33 K for a 10 mm thickness. This radiation temperature is higher than that of the adjacent clothed human skin, so this appears darker, by about 0.57 K than the adjacent clothed body, as shown in Figure 8. However, for a 5 mm thickness, this material has a radiation temperature 0.34 K lower than the surrounding body, as indicated in Table I.

4) YELLOW BEESWAX

Yellow beeswax is a convenient surrogate for a class of nitrogen-based energetic materials. Reference [53] shows it to have a relative permittivity of (2.36, 0.015) which generates the radiation temperature of 302.51 K for a thickness of 10 mm, but a radiation temperature of 302.62 K for a thickness of 5 mm. These radiation temperatures are slightly lower than the radiation temperature of the surrounding human body, which has a radiation temperature of 302.76 K.

5) WATER PACK

Properties are also shown for a 10 mm thick water pack. Although this material is not a threat by itself, it could be used to conceal a threat, as it is non-transmissive and has properties similar to that of the human body. It has been assumed that the water pack has the same relative permittivity as water, which at a temperature of 302.0 K has a value of (48.7085, 32.7862) using the model of Mätzler [54]. The water pack appears with a radiation temperature of 297.91 K, lower than that of the body as it is quite reflective and has a lower thermodynamic temperature than the human body.

C. *THREATS IN CANYON REGIONS*

A challenging area for security screening is the detection of objects in bodily canyon regions. An example of this is illustrated in Figure 9, where a 10 cm long, 1.6 mm thick ceramic bladed weapon in the armpit is shown in the HL, VL, and circular polarization.

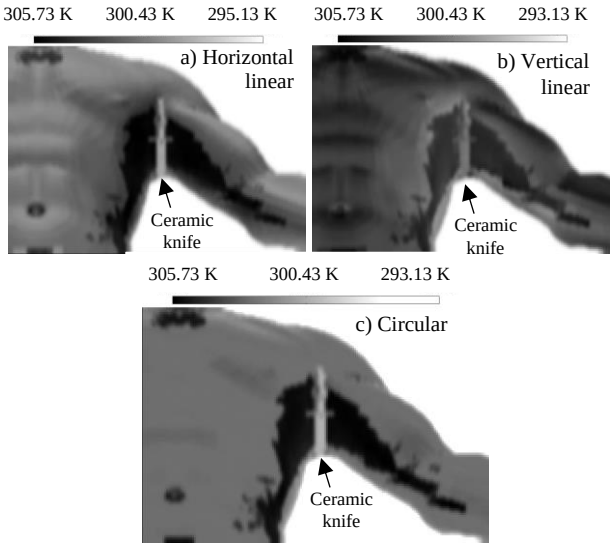

FIGURE 9. The simulated image of the ceramic knife in the armpit showing (clockwise from the top left) the effects in a) horizontal linear, b) vertical linear and c) circular polarization. Circular polarization offers the least clutter due to the absence of Brewster angle effects.

In the HL and VL polarizations, variations in the radiation temperatures over the curvatures of the skin can be observed. In the image of the circular polarization, the variations are much reduced and this makes recognition of the knife in the armpit easier. In the circular polarization, the ceramic knife has a radiation temperature of 299.88±0.05 K, whilst the adjacent body radiation temperature in the canyon region has a value of 304.50±0.05 K, and just outside the canyon region it has a value of 302.04±0.05 K.

IV. SUPPORTING EXPERIMENTAL MEASUREMENTS

Experimental measurements were made using a radiometer measuring left-hand circular polarization at 20 GHz. The system was calibrated and used to reproduce the results shown in Table I for comparison.

A. *MEASUREMENT SYSTEM DESCRIPTION*

This radiometer was built around a commercially available (Triax TWIN KA TKT 001) K band satellite receiver low noise block (LNB) downconverter. These LNBs use a stepped septum-type waveguide circular polarizer [55] in the front-end feed to divide input radiation into channels for

left(right)-hand circular polarizations. Electronics in the module enable the amplified power in these polarizations to be passed to the output F-connectors. The left-hand (right-hand) circular polarization signal is selected by the application of 13 V (18 V) direct current voltage to the LNB via the bias-T. The LNB has an internal local oscillator at 21.2 GHz and is designed to be sensitive over the band from 19.7-20.2 GHz. Previous work using X band (10 GHz) LNBs showed them to be effective both as direct detection radiometers and as an interferometer as used in aperture synthesis imaging [56].

A photograph and a schematic of the 20 GHz radiometer including the data acquisition system is shown in Figure 11. A bias-T connector is used to supply the 13 V to the LNB to select the left-hand circular (LC) polarization and to power the in-line Axing SVS 2-01 coaxial (20 dB gain) intermediate frequency (IF) amplifier. A variable (0-20 dB) SAC AE5199DC coaxial attenuator is used to set power levels, to avoid the non-linear detector regime and have convenient voltage levels for the data acquisition. An envelope detector, sensitive over the band 0.1 MHz to 3.3 GHz, is DC coupled via a lowpass filter having a cut-off frequency of 1 kHz (manufacturers specification) to an Owon multimeter (model B35T+) to measure output voltages. The coaxial attenuator is adjusted to set the output voltages to ~55 mV for ambient temperature emission into the LNB feed. The multimeter samples the detector output voltages approximately twice per second with a resolution of 10 μV and with an unspecified amount of low-pass filtering. The data is then transferred to the mobile phone for spread-sheet storage and display. Since the components are sourced from the satellite comms and Wi-Fi market, they are readily available and relatively inexpensive: LNB (50$), coaxial amplifier (8$), bias-T ($4), variable attenuator ($10), power supply unit ($10), connectors & cables ($10), multimeter ($35). Some of these components could even be included in the front-end of a proof-of-concept portal aperture synthesis demonstrator imager.

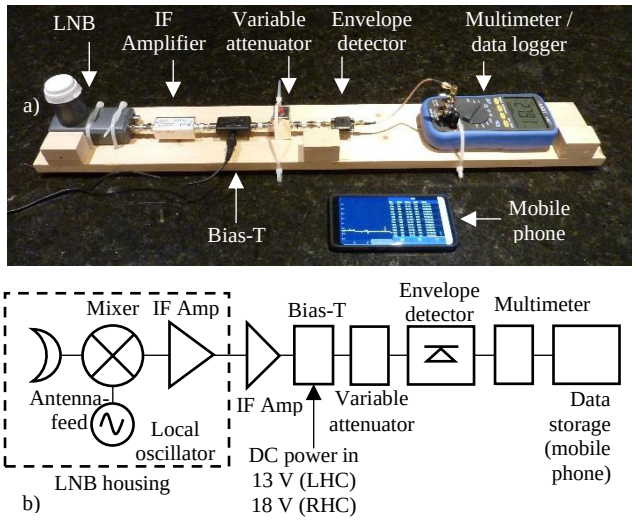

FIGURE 11. The 20 GHz circular polarization radiometer constituent parts, showing: a) a photograph b) a schematic of the circuit. From left to right: LNB, in-line IF amplifier, bias-T (with DC power line), envelope detector, with multimeter data logger blue-toothed to a Samsung S10+ mobile phone (below) for storage and display.

B. *SYSTEM PERFORMANCE*

Performance measurements on the 20 GHz radiometer indicate it has a receiver noise temperature of 134 K and that thermal radiation in the K band is down-converted into the intermediate frequency band covering the range from 15 MHz to 2.4 GHz, so the system may well have a radiation bandwidth larger than that specified for its use as a satellite receiver. The system has a warm-up time of about 40 minutes, during which time the detector output voltage falls by about 7%, before becoming stable.

C. *SYSTEM CALIBRATION*

Calibration of the radiometer was made using emission from the surfaces of two millimeter-wave absorbers, one at ambient room temperature and the other at an elevated temperature, by attachment to a domestic heating radiator. The thermodynamic temperatures of the surfaces were measured using a Metene FR-200 instrument, a medical non-contact infrared thermometer (NCIT). This device measures with an accuracy of ±0.3°C, with a resolution of 0.1°C. During these measurements there was stability in the ambient room and radiator mounted absorber temperature, these being 22.0°C and 36.0°C respectively. This calibration method is very similar to that method described in [44] used for measuring the microwave properties of human skin. The calibration indicated the responsivity to be ~0.11 mV/K, which given the multimeter resolution of 10 μV, gives a radiation temperature measurement resolution of ~0.09 K. This is borne out in the time traces of radiation temperatures of the calibration sources as measured by the multimeter and an oscilloscope.

An estimated minimum detectable radiation temperature variation is 0.096 K from the radiometer equation (3), assuming a receiver noise temperature of 134 K, an antenna radiation temperature of 295.15 K (273.15 K + 22.0°C), a radiation bandwidth of 2 GHz and a 10 ms integration time. This figure is close to that above measured. It may be improved upon by better filtering before sampling.

D. *MEASUREMENT PROCEDURE*

Indoor measurements of the radiation temperatures of the human skin and skin covered with a thin layer of clothing were made, by placing objects ~10 cm away from the LNB feed horn. However, when objects were placed at this proximity the apparent noise level on the data increased from 0.1 K to about 0.3 K. This limits the sensitivity of the system at very close range and this may be caused by the object affecting the electrical performance of the feed horn. Alternatively, it may be caused by radiation exiting the

feedhorn being back-scattered from the object, and re-entering the receiver, as reported in other close-in measurements [18].

E. *MEASUREMENT RESULTS*

Objects to be measured were placed between the skin and clothing to mimic the scenario depicted in Figure 4b. Objects measured in this way were: metal, carbon fiber (1.1 mm thick), ceramic knife (blade: 20 cm long x 1.6 mm thick), yellow beeswax (17.5 cm diameter x 10 mm thick) and a water-filled sealable plastic bag having a thickness of ~20 mm. A photograph of the objects is shown in Figure 12. The measured thermodynamic temperatures and radiation temperatures are shown in Table II. It can be appreciated that the radiation temperatures of the threat materials are within a few degrees Kelvin of the radiation temperature of the human body, showing good agreement with the simulated radiation temperatures of Table I.

FIGURE 12. The materials that have been measured using the 20 GHz radiometer of Figure 11. From the top: the water pack (left), the yellow beeswax (right), the carbon fiber, and the ceramic. In the case of the ceramic, a larger surface area was created by fixing four (20 cm long bladed) ceramic knives together.

In the case of the ceramic and the carbon fiber, these materials were also measured separately to obtain information about their properties. The knife blade, which had a length of 150 cm, a width of 3.3 cm, and a thickness of 1.6 mm (at its thickest part), was heated by placing in boiling water. It was then placed directly in front of the LNB feedhorn and the measured radiation temperature only increased by a small amount indicating the emissivity was in the region of 0.02. The same knife was then placed directly in front of the LNB as the system was pointed to the zenith sky on a clear day (which has an estimated radiation temperature of 35 K). This indicated the transmittance was ~0.31. Since the transmittance, emissivity, and reflectance sums to unity, this gives a value of 0.67 for the reflectance which is similar to that estimated from the material properties.

Similarly, the transmittance, emissivity, and reflectance of the carbon fiber were measured, giving a result of 0.14, 0.01, 0.85 respectively. Agreement with that value from Table I is less good, suggesting that the permittivity of the sample material is higher than that indicated in the table.

Detailed measurements were not made using the RC polarization (by applying 18 V to the LNB), but the overall response in this polarization was similar, as was the receiver noise temperature.

TABLE II
MEASURED RADIATION TEMPERATURES OF THREAT MATERIALS FROM TABLE I IN THE CONFIGURATION DEPICTED IN FIGURE 4 FOR AN AMBIENT TEMPERATURE OF 22°C (295.15 K) AND A SKIN TEMPERATURE OF 35.7°C (308.85 K).

Material	Thermodynamic Temperature	Radiation Temperature	Radiation temperature difference (threat – background)
Bare skin	308.85 K (35.7°C)	302.50±0.15K	N.A.
Thin clothing over the skin (background)	300.75 K (27.6°C)	302.50±0.15 K	0.00 K
Metal	304.45 K (31.3°C)	296.70±0.15 K	-5.80±0.30 K
Carbon fiber 1.1 mm thick	296.15 K (23.0°C)	296.80±0.15 K	-5.70±0.30 K
Ceramic (ZrO_2) 1.6 mm thick	296.15 K (23.0°C)	296.90±0.15 K	-5.60±0.30 K
Beeswax 10 mm thick	299.35 K (26.2°C)	301.30±0.15 K	-1.20±0.30 K
Water pack 20 mm thick	308.65 K (35.5°C)	301.40±0.15 K	-1.10±0.30 K

F. *DISCUSSION ON MEASUREMENT AND SIMULATION*

The differences in the radiation temperatures displayed in Table II show small values (< 7 K) which are in general agreement with the results of the simulations shown in Table I. However, the measured differences in the radiation temperatures of the metal, carbon fiber and ceramic were all slightly greater than the simulated differences and are outside the experimental error. In the case of the metal, this might be explained by the relative permittivity of the skin being larger than that indicated in Table I and used in the simulation. At a frequency of 20 GHz, the penetration of the microwave radiation into the skin might be such that tissue other than skin is being reached, which is likely to contain higher levels of water, which would raise the reflectivity. This would reduce the difference in the simulated radiation temperatures toward that of the measurement. In the case of the carbon fiber and ceramic, the relative permittivities may indeed be larger than those assumed in Table I; a higher value of permittivity would increase the radiation temperature toward that of the measured value.

In the case of the beeswax, the measured radiation temperature difference is just slightly greater than the simulation. This might be explained by incorrect values of both the permittivity of the skin and the beeswax used in the

simulation. Small changes here would bring measurements in line with simulation.

Results for water pack show a measured radiation temperature difference less than that of the simulation. This could be explained by the reflectivity of the human body being higher than that of the skin. As in the case of the metal, this may be happening as the 20 GHz radiation penetrates to regions of tissues where increased water content gives higher reflectivities. If a higher permittivity would be taken for the body tissue, this would reduce the difference in the simulated radiation temperature differences.

What these simulations and measurements show is that the radiation contrast of threats against the body is smaller than 7 K and that there are subtle changes at the sub-Kelvin level that arise due to radiometric cavity fringes for varying thicknesses of threat materials. It can be seen from Table I that variations exist at the hundreds of millikelvin level for the differing threats, so the only way to guarantee the detection of these with low false alarm rates is if the radiometric sensitivity of a security screening portal is in the 100 mK region.

V. NEXT STAGES OF PORTAL DEPLOYMENT

Aperture synthesis hardware for a future security screening portal comprises an antenna-receiver array (as depicted in Figure 3), a cross-correlator, and a machine learning processor linked to a security network, as illustrated in Figure 13. The antenna array will be based on a minimally redundant array with some randomization of antenna positions, as discussed in the earlier section on antenna array topology.

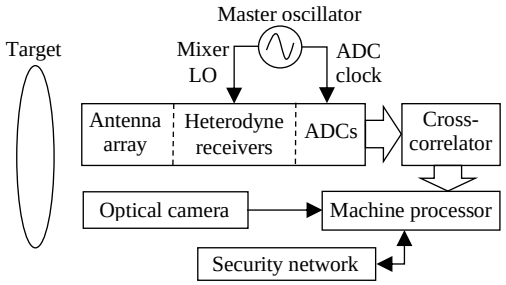

FIGURE 13. A schematic of the envisaged security screening portal, showing the antenna-receiver array, a cross-correlator, and a machine learning processor, with a communication link to the infrastructure security network. The master oscillator provides the local oscillator (LO) for the heterodyne receivers and the clock for the analog-to-digital converters (ADCs).

The heterodyne receivers of Figure 13 amplify and filter the radiometric emission collected by the antenna, with a phase lock to a master oscillator. The phase lock ensures coherence in the measured radiometric emission across all receiver channels, this being necessary for image reconstruction as discussed in [20]. The LNBs discussed earlier in this document could form part of the receiver, injecting an external local oscillator (LO) into the mixer to ensure phase coherence over the array, as demonstrated in [56]. Since radiation bandwidths in excess of a few hundred MHz are necessary to achieve radiometric sensitivity (as indicated in Eq. 3), the Nyquist sampling rate (at twice this bandwidth) is currently very challenging to achieve using long-word (> 4 bits) analog-to-digital converters (ADCs). Fortunately, however, when measuring radiometric emission, sampling using a comparator as a single-bit ADC is possible [10], which brings the costs of these components down considerably.

A. *CROSS-CORRELATORS*

The cross-correlator is an essential subsystem of an aperture synthesis imaging system [10]. Cross-correlators have a long history of development in the field of radio astronomy. The action of the cross-correlator is to perform a conjugate cross-multiply of the sampled electric fields from all pairs of receiver channels. Initially, correlators were built from analog electronics and capable of processing signals from small numbers of receiver channels having megahertz bandwidths. However, correlators today, built for radio astronomy, are far more powerful digital systems, capable of processing tens of receiver channels, having bandwidths of several GHz [14], [57].

Digital correlators offer a great benefit, as most of the electronic complexity is contained within the silicon processor, that being a Field Programmable Gate Array (FPGA) [58], a Graphics Processor Unit (GPU) [59], [60], or an Application Specific Integrated Circuit (ASIC) [13]. This miniaturizes hugely the physical size of the correlator, as the number of electrical cables, joining discrete electronic components, is minimized. The compactness this offers means the correlator can be integrated with the antenna-receiver circuit boards, enabling the portal to be conformally deployed in the confined spaces of entrances for security screening.

The electronic complexity of a correlator is proportional to the square of the number of receiver channels [14]. This is particularly a challenge for the aperture synthesis portal, as hundreds of channels are required. This has considerable implications for non-recurring engineering costs, as digital cross-correlators are not commercially available off-the-shelf items. These systems are generally designed and built by a relatively small community of workers, highly skilled in the development of high-speed (gigabit per second) embedded technology.

B. *MACHINE PROCESSOR*

In the machine processor, algorithms based on Fourier transforms and matrix multiplies generate the imagery [61]. Algorithms outlined in [22] enable the Gerchberg technique to improve the aperture synthesis image by using the positional data of the subject in the portal from an optical camera. Alternatively, this technique could be used to provide the same quality of image for a reduced number of receiver channels. This would offer an attractive cost saving,

since optical cameras are less expensive than channels in an aperture synthesis system. The final image generated by these algorithms is a surface of the human body in three-dimensional space, which would be analyzed by machine for potential threat items. The thickness of this surface would be of the order of the half-wavelength resolution (7.5 mm at a 20 GHz radiation frequency), as the radiation propagates only a fraction of a millimeter into the skin and the clothing is almost transparent.

For a non-invasive, potentially non-cooperative, screening capability, it is desirable to screen a walking subject. Furthermore, in imaging a walking person it becomes more difficult to conceal threats or illegal items from view. This is because in the walking scenario more regions of the body can be viewed from different directions, giving criminals fewer opportunities to conceal objects on regions of the body that are not screened well by the static pose systems.

Blurring in aperture synthesis imagery can be avoided, since image integration times can be shorter than the timescale of physical movements (milliseconds). However, unless extremely large radiation bandwidths are used, these short integration times lead to noisy images. Fortunately, the use of the optical camera to determine the locations of different regions of the body will enable multiple 3-D images, recorded during the transit of the portal, to be combined into a single high-quality image.

Since the 1950s there has been a constant stream of research into the microwave and millimeter-wave properties of materials, including those of threats, clothing, and the human body. In particular, the variation in the reflectance of human skin is now better understood, this being shown to vary with body region, gender, age, and ethnicity [43]. This information puts the radiation temperature of the skin of the human body in a narrow band, making it possible to determine if it is indeed human skin that is being imaged or a potential threat item. Using the radiation temperature of the potential threat and its shape it may be possible to make a classification of the object.

A priority at security checkpoints is that the screening process does not lead to a bottleneck of people. This means the image acquisition and analysis process must be quicker than the rate at which people arrive. To avoid a bottleneck, the complete screening process needs to be shorter than 750 ms, if people are spaced 1 m apart and walking toward the portal at a speed of 1.5 m/s. Given the detail in an image and the short timescales involved, the analysis of imagery is only possible using a machine.

C. *FOLLOW-ON HIGHER TRL SYSTEMS*

The next stage is to develop a TRL 5 aperture synthesis imager (following the TRL 4 system [20]), a system to demonstrate security screening capabilities in a simulated operational environment. The system will have several hundred receiver channels and have a radiometric sensitivity in the region of 0.5 K at 10 image frames per second. The system will image one side of the human torso, a curved surface having an area of approximately half a square meter. With a half-wavelength spatial resolution of 7.5 mm (at 20 GHz) it will generate approximately 9000 pixels. This system will be a testbed for demonstrating the three-dimensional imaging algorithms simulated in [22] and will trial the Gerchberg technique for enhancing image quality and reducing the number of antenna-receiver channels in the array.

A follow-on TRL 6 system would be one that could image a complete human torso from all directions in 3-D in a simulated security screening environment. From TRL 6 onwards, working with government departments responsible for equipment certification would ensure products based on the design could enter the security screening markets unimpeded.

The TRL 7 system would be a prototype product that could image in 3-D the full human body in an operational security screening environment. With the average surface area of the body being ~1.9 m^2, this system would generate approximately 35,000 pixels over the surface with a 7.5 mm spatial resolution. A successful TRL 7 prototype would be developed further by industry and taken to market. It is expected that with appropriate funding, the development of each of the above TRL systems would be a 2-year project.

VI. CONCLUSIONS

The challenges facing the development of an indoor security screening portal have been quantified in terms of the contrasts in the radiation temperatures of threats concealed under clothing against the human body. Using the information on the transmission of clothing and the relative permittivities of human skin and several threat materials the radiation temperature of the clothed human body and the concealed weapons has been calculated for an operational frequency of 20 GHz.

Materials that have been evaluated are metal, ceramic, carbon fiber, RDX, yellow beeswax, and a water pack. A coherent and an incoherent layer model of the clothed human and the threats have been used. The results are presented in tabular form and as a scene simulation. Simulations indicate the benefits of using circular polarization as a means of reducing the false alarm rate and that radiometric cavity fringes can contribute to the signature of a threat. The scene simulations show canyon effects, where multiple reflections increase radiation temperatures in areas such as between the legs and in the armpits. A simulation is also shown of how a ceramic knife appears when concealed in the armpit.

Measurements of materials under clothing against the skin have been conducted with a 20 GHz radiometer measuring left-hand circularly polarized radiation. The measurements show reasonable agreement with the simulation in that the contrasts of threats against the body are all below ~7 Kelvin. Some of the contrasts are down to a Kelvin, with the limiting contrast measurable being in the region of 0.3 Kelvin using the system presented here. Simulations indicate the signatures exist below this level and that for a security

screening portal to function effectively the radiometric sensitivity needs to be in the region of around 100 millikelvin.

Realization of a radiometric imaging technology whereby all regions of the human body can be in focus in the near-field regime of a security screening portal is possible using an aperture synthesis imaging system [11]. However, such a system can only be realized by accessing low-cost multichannel radiometric digital receivers interfaced with digital cross-correlators [12], [13], [14].

REFERENCES

[1] D. M. Sheen, D. L. McMakin, and T. E. Hall, "Three-Dimensional Millimeter-Wave Imaging for Concealed Weapon Detection," *IEEE Transactions on Microwave Theory and Techniques,* vol. 49, no. 9, pp. 1581-1592, September 2001.

[2] S. S. Ahmed, A. Schiessl, and L.-P. Schmidt, "A Novel Fully Electronic Active Real-Time Imager Based on a Planar Multistatic Sparse Array," *IEEE Transactions on Microwave Theory and Techniques,* vol. 59, no. 12, pp. 3567-3576, December 2011.

[3] D. T. Hodges, E. E. Reber, F. B. Foote, and R. L. Schellenbaum, "Safeguards applications of far infrared radiometric techniques for the detection of contraband," *Nuclear Materials Management,* vol. 8, no. 4, pp. 75-95, 1980.

[4] E. E. Reber, F. B. Foote, R. L. Schellenbaum, and R. G. Bradley, "Evaluation of Active and Passive Near Millimeter-Wave Radiometric Imaging Techniques for Detection of Concealed Objects," Department of Commerce National Technical Information Service DE81031938, SAND-81-1051 Sandia National Laboratories, Albuquerque, July 1981.

[5] P. F. Goldsmith, C.-T. Hsieh, and G. R. Huguenin, "Focal Plane Imaging Systems for Millimeter Wavelengths," *IEEE Transactions on Microwave Theory and Techniques,* vol. 41, no. 10, pp. 1664-1675, October 1993.

[6] A. Pergande and L. T. Anderson, "Video-rate millimeter-wave camera for concealed weapons detection," in *Passive Millimeter-Wave Imaging Technology V*, Orlando, August 2001.

[7] C. Mann, "Practical Challenges for the Commercialisation of Terahertz Electronics," in *IEEE/MTT-S International Microwave Symposium*, Honolulu, June 2007.

[8] P. Helisto, A. Luukanen, L. Gronberg, J. S. Penttila, H. Seppa, H. Sipola, and C. R. Dietlein, "Antenna-coupled microbolometers for passive THz direct detection imaging arrays," in *Proceedings of the 1st European Microwave Integrated Circuits Conference*, Manchester, September 2006.

[9] N. Alexander, C. Callejero, F. Fiore, I. Gomez, R. Gonzalo, A. E. de Luna, I. Ederra, and I. Palacios, "Mm-wave stand-off screening and detection," in *International Conference on Electromagnetics in Advanced Applications,* Torino, September 2009.

[10] A. R. Thompson, J. M. Moran, and G. W. Swenson, Interferometry and Synthesis in Radio Astronomy, 2 ed., Weinheim: Wiley-VCH, 2004.

[11] N. A. Salmon, "3-D Radiometric Aperture Synthesis Imaging," *IEEE Transactions on Microwave Theory and Techniques,* vol. 63, no. 11, pp. 3579-3587, November 2015, DOI: 10.1109/TMTT.2015.2481413.

[12] X. Guo, M. Asif, A. Hu, Z. Li, and J. Miao, "A 1-GHz 64-Channel Cross-Correlation System for Real-Time Interferometric Aperture Synthesis Imaging," *MDPI Sensors 2019,* vol. 19, no. 1739, pp. 1-13, 2019.

[13] E. Ryman, A. Emrich, S. B. Andersson, L. Svensson, and P. Larsson-Edefors, "1.6 GHz Low-Power Cross-Correlator System Enabling Geostationary Earth Orbit Aperture Synthesis," *IEEE Journal of Solid-State Circuits,* vol. 49, no. 11, pp. 2720-2729, November 2014.

[14] D. C. Price, J. Kocz, M. Bailes, and L. J. Greenhill, "Introduction to the Special Issue on Digital Signal Processing in Radio Astronomy," *Journal of Astronomical Instrumentation,* vol. 5, no. 4, p. 1602002 (11 pages), December 2016.

[15] M. Bass (Ed.), R. Oldenbourg, and M. Shribak, "Microscopes, Chapter 28," in *Handbook of Optics, vol. 1*, McGraw Hill, 2010, pp. 28.1-28.62.

[16] N. A. Salmon, N. Bowring, S. Hutchinson, M. Southgate, and D. O'Reilly, "An aviation security (AVSEC) screening demonstrator for the detection of non-metallic threats at 28-33 GHz," in *Proc. SPIE vol. 8900, ESD, Millimetre Wave Terahertz Sensors and Technology, VI*, Dresden, October 2013, DOI: 10.1117/12.2030795.

[17] N. J. Bowring, D. O'Reilly, N. A. Salmon, D. A. Andrews, N.-D. Rezgui, S. W. Harmer, "A feasibility study into the screening and imaging of hand luggage for threat items at 35 GHz using an active large aperture (1.6 m) security screening imager," in *Proc. SPIE vol. 8900, ESD, Millimetre Wave and Terahertz Sensors and Technology VI*, Dresden, October 2013, DOI: 10.1117/12.2030835.

[18] N. A. Salmon, L. Kirkham, and P. N. Wilkinson, "Characterisation and calibration of a large aperture (1.6 m) ka-band indoor passive millimetre wave security screening imager," in *SPIE ESD*, Edinburgh, October 2012, DOI: 10.1117/12.999278.

[19] H. Eyal and R. Daisy, "Three dimensional real time ultra-wide band whole body imaging system," in *IEEE Radar Conference*, Atlanta, May 2012.

[20] N. A. Salmon, R. Macpherson, A. Harvey, P. Hall, S. Hayward, P. Wilkinson, and C. Taylor, "First video rate imagery from a 32-channel 22-GHz aperture synthesis passive millimetre wave imager," in *Proc. SPIE vol. 8188, ESD, Millimetre Wave Sensors and Technology IV*, Prague, October 2011, DOI: 10.1117/12.899564.

[21] C. Zheng, X. Yao, H. Anyong, and J. Miao, "A Passive Millimeter-Wave Imager used for Concealed Weapon Detection," *PIERS B,* vol. 46, pp. 379-397, 2013, DOI:10.2528/PIERB12101505.

[22] N. A. Salmon, "Extended sources near-field processing of experimental aperture synthesis data and application of the Gerchberg method for enhancing radiometric three-dimensional millimetre-wave images in security screening portals," in *Proc. SPIE vol. 10439, ESD, Millimetre Wave Terahertz Sensors and Technology X*, Warsaw, October 2017, DOI: 10.1117/12.2282563.

[23] N. A. Salmon, "Outdoor Passive Millimeter-Wave Imaging: Phenomenology and Scene Simulation," *IEEE Transactions on Antennas and Propagation,* vol. 66, no. 2, pp. 897-908, February 2018, DOI: 10.1109/TAP.2017.2781742.

[24] N. A. Salmon, "Passive millimeter wave imagers for safety and security," SPIE Newsgroup, 27 August 2008. [Online]. Available: https://spie.org/news/1236-passive-millimeter-wave-imagers-for-safety-and-security.

[25] J. Yinon, Counterterrorist detection techniques of explosives, Amsterdam: Elsevier, 2007.

[26] B. Trumbore and T. Moeller, "Fast, Minimum Storage Ray-Triangle Intersection," *Journal of Graphics Tools,* vol. 2, no. 1, pp. 21-28, January 1997.

[27] N. A. Salmon, "Polarimetric passive millimetre-wave imaging scene simulation including multiple reflections of subjects and their backgrounds," in *Proc. vol. 5989, ESD, Passive Millimetre-Wave and Terahertz Imaging II*, Bruges, November 2005, DOI: 10.1117/12.634443.

[28] A. Luukanen, R. Appleby, M. Kemp, and N. Salmon, "Millimeter-Wave and Terahertz Imaging in Security Applications," in *Terahertz Spectroscopy and Imaging*, Berlin Heidelberg, Springer-Verlag, 2013, DOI: 10.1007/978-3-642-29564-5_19, pp. 491-520.

[29] L. E. Kopilovich and L. G. Sodin, Multielement system design in astronomy and radio science, Dordrecht: Springer-science+business media, 2001.

[30] L. G. Sodin and L. E. Kopilovich, "Aperture-synthesis systems with complete coverage of a hexagonal domain in the (U,V) plane,"

Radiophysics and Quantum Electronics, vol. 43, no. 4, pp. 312-316, April 2000.

[31] N. A. Salmon, P. Wilkinson, and C. Taylor, "Interferometric aperture synthesis for next generation passive millimetre wave imagers," in *Proc. SPIE 8544, Millimetre Wave and Terahertz Sensors and Technology V*, Edinburgh, October 2012, DOI: 10.1117/12.931115.

[32] D. Zhu, F. Hu, L. Lang, P. Tang, X. Peng, and F. He, "Radiometric Sensitivity and Angular Resolution Optimisation of Thinned Linear Arrays in Microwave Interferometric Radiometry," *IEEE Transactions on Antennas and Propagation*, vol. 67, no. 1, pp. 568-573, January 2019.

[33] D. Zhu, F. Hu, X. Peng, and H. Lu, "On Baseline Weighting for Radiometric Sensitivity Analysis in Microwave Interferometric Radiometry," *IEEE Antennas and Wireless Propagation Letters*, vol. 18, no. 4, pp. 791-795, April 2019.

[34] D. Zhu and X. Peng, "Combinatorial Design of Low-Degradation Linear Arrays in Interferometric Aperture Synthesis Radiometers," *IEEE Transactions of Antennas and Propagation*, vol. 67, no. 12, pp. 7340-7347, December 2019.

[35] N. A. Salmon, R. Appleby, and P. Coward, "Polarimetric passive millimetre wave imaging," in *SPIE vol. 4373, Passive Millimeter-Wave Imaging Technology V*, Orlando, August 2001, DOI: 10.1117/12.438147.

[36] M. Link, C. Montzka, T. Jagdhuber, S. S. Sobjærg, S. Dill, M. Peichl, T. Meyer, and F. Jonard, "Impact of permittivity patterns on fully polarimetric brightness temperature signatures at L-band," *Progress in Electromagnetics Research*, vol. 166, pp. 75-93, 2019, DOI:10.2528/PIER19080204.

[37] F. T. Ulaby, R. K. Moore, and A. K. Fung, Microwave Remote Sensing - Active and Passive, Volume 1, Norwood: Artech House, 1981.

[38] N. A. Salmon, "Polarimetric scene simulation in millimetre wave radiometric imaging," in *SPIE Proc. vol. 5410, Passive Millimeter Wave Imaging Technology VII*, Orlando, August 2004, DOI: 10.1117/12.562206.

[39] N. A. Salmon and P. R. Coward, "Scattering in polarimetric millimetre-wave imaging scene simulation," in *Proc. vol. 6211, Passive Millimeter-Wave Imaging Technology IX*, Orlando, May 2006, DOI: 10.1117/12.669049.

[40] C. Gabriel, S. Gabriel, and E. Corthout, "The dielectric properties of biological tissues: I. Literature survey," *Physics in Medicine & Biolology*, vol. 41, pp. 2231-2249, November 1996.

[41] S. Gabriel, R. W. Lau, and C. Gabriel, "The dielectric properties of biological tissues: III. Measurements in the frequency range 10 Hz to 20 GHz," *Physics in Medicine & Biology*, vol. 41, pp. 2271-2293, November 1996, DOI:10.2528/PIER19080204.

[42] S. Gabriel, R. W. Lau, and C. Gabriel, "The dielectric properties of biological tissues: II. Measurements in the frequency range 10 Hz to 20 GHz," *Physics in Medicine & Biology*, vol. 41, pp. 2251-2269, November 1996.

[43] W. D. Hurt, "Radiofrequency radiation dosimetry workshop," Brooks Air Force Base, Internal Report, no. AL/OE-SR-1996-0003, San Antonio, 1996.

[44] A. Y. Owda, N. Salmon, S. W. Harmer, S. Sergiy, N. J. Bowring, N.-D. Rezgui, and M. Shah, "Millimeter-Wave Emissivity as a Metric for the Non-Contact Diagnosis of Human Skin Conditions," *Bioelectromagnetics*, vol. 38, pp. 559-569, DOI: 10.1002/bem.22074, October 2017.

[45] J. E. Bjarnason, T. L. J. Chan, A. W. M. Lee, M. A. Celis, and E. R. Brown, "Millimeter-wave, terahertz, and mid-infrared transmission through common clothing," *Applied Physics Letters*, pp. 519-521, 26th July July 2004.

[46] N. Alexander, C. Callejero, and R. Gonzalo, "Millimetre-wave materials properties," in *Joint 32nd International Conference on Infrared and Millimeter Waves and the 15th International Conference on Terahertz Electronics*, Cardiff, September 2007.

[47] Z. Xiao, J. Xu, and T. Hu, "Research on the Transmissivity of Some Clothing at Millimeter-wave Band," in *ICMMT 2008 International Conference on Microwave and Millimeter Wave Technology*, Nanjing, April 2008.

[48] R. Appleby and H. B. Wallace, "Standoff Detection of Weapons and Contraband in the 100 G Hz to 1 THz Region," *IEEE Transactions on Antennas and Propagation*, vol. 55, no. 11, pp. 2294-2956, November 2007.

[49] S. W. Harmer, N. Rezgui, N. Bowring, Z. Luklinska, and G. Ren, "Determination of the Complex Permittivity of Textiles and Leather in the 14-40 GHz, mm wave band using a Free-Wave Transmittance Only Method," *IET Microwaves, Antennas & Propagation*, vol. 2, no. 6, pp. 606-614, September 2008.

[50] T. Zou, N. Zhao, and J. Li, "Microwave absorbing properties of activated carbon fibre polymer composites," *Bulletin of Materials Science*, vol. 34, no. 1, pp. 75-79, February 2011.

[51] D. Min, N. Hoivik, G. U. Jensen, F. Tyholdt, C. Haavik, and U. Hanke, "Dielectric properties of thin-film ZrO2 up to 50 GHz for RF MEMS switches," *Applied Physics A 105*, pp. 867-874, December 2011.

[52] A. L. Higginbotham Duque, W. L. Perry, and C. M. Anderson-Cook, "Complex Microwave Permittivity of Secondary High Explosives," *Propellants, Explosives, Pyrotechnics*, pp. 275-283, 2014.

[53] A. R. von Hippel, Dielectric Materials and Applications, New York: Wiley, 1954.

[54] C. Mätzler, "Dielectric properties of natural media (Chapter 5)," in *Thermal Microwave Radiation: Applications for Remote Sensing*, Stevenage, IET, 2006.

[55] J. Bornemann and V. A. Labay, "Ridge Waveguide Polarizer with Finite and Stepped-Thickness Septum," *IEEE Transactions on Microwave Theory and Techniques*, vol. 43, no. 8, pp. 1782-1787, August 1995.

[56] N. A. Salmon, P. N. Wilkinson, and J. Radiven, "Amplitude and intensity interferometry using satellite LNB receivers for innovative and low cost microwave and millimetre wave sensor development," in *SPIE Proc. vol. 8544, ESD, Millimetre Wave and Terahertz Sensors and Technology V*, Edinburgh, October 2012, DOI: 10.1117/12.978643.

[57] J. Hickish et al, "A Decade of Developing Radio-Astronomy Instrumentation using CASPER Open-Source Technology," *Journal of Astronomical Instrumentation*, vol. 5, no. 4, p. 1641001 (24 pages), 2016.

[58] J. Kocz et al, "A Scalable Hybrid FPGA/GPU FX Correlator," *Journal of Astronomical Instrumentation*, vol. 3, no. 1, p. 1450002 (10 pages), March 2014.

[59] J. Kocz et al, "Digital Signal Processing Using Stream High Performance Computing: A 512-Input Broadband Correlator For Radio Astronomy," *Journal of Astronomical Instrumentation*, vol. 4, no. 1 & 2, p. 1550003 (12 pages), June 2015.

[60] P. C. Broekema, J. J. D. Mol, R. Nijboer, A. S. van Amesfoort, M.A. Brentjens, G. M. Loose, W.F.A. Klijn, and J. W. Romein, "Cobalt: A GPU-based correlator and beamformer for LOFAR," *Astronomy and Computing*, vol. 23, pp. 180-192, April 2018.

[61] N. A. Salmon and N. Bowring, "Simulations of three-dimensional radiometric imaging of extended sources in a security screening portal," *Proc. SPIE*, vol. 9651, p. (7 pages), October 2015.